A Dual-Band Dual-Output Power Amplifier for Carrier Aggregation

Tommaso Cappello, *Member, IEEE*, Allison Duh, *Student Member, IEEE*, Taylor Wallis Barton, *Member, IEEE*, and Zoya Popovic, *Fellow, IEEE*

***Abstract*— This paper demonstrates a high-efficiency dual-band RF power amplifier (PA) for sub-6 GHz 5G carrier aggregation. The dual-band PA is tested with modulated signals generated by a new algorithm designed to provide realistic waveforms for carrier aggregation scenarios, allowing flexible complex (IQ) modulated sequences with arbitrary peak-to-average power ratio (PAPR), bandwidth, and band distribution. A single-stage PA is designed with a packaged 6-W transistor and a diplexer-like output matching network that separates the two bands into two outputs. It achieves an output power of 36.7 and 37.1 dBm and a power-added efficiency (PAE) of 40.4% and 39.9% at 3.5 and 5.5 GHz, respectively. Under concurrent, dual-band drive with 10-MHz, 6-dB PAPR signals and with digital predistortion applied to varying frequency notch bandwidths, an average PAE of 25.6%, a normalized mean square error of 2.4%/1.0%, and an adjacent channel power ratio of −46.8/−48 dBc in the two bands (3.5/5.5 GHz) is measured.**

***Index Terms*— Carrier aggregation, concurrent operation, digital predistortion (DPD), dual band, gallium nitride (GaN), Long Term Evolution (LTE) Advanced, multiband, multitone, peak-to-average power ratio (PAPR), power amplifier (PA).**

I. Introduction

THE need for efficient RF transmitters capable of concurrent multisignal amplification is increasing due to the development of 5G systems, characterized by increased spectral efficiencies and instantaneous signal bandwidths [1]–[4]. Several complex signal scenarios are anticipated, including carrier aggregation of Long Term Evolution (LTE)-like signals [5]. Carrier aggregation increases overall required bandwidth by utilizing several bands within the available spectrum, aggregated contiguously, noncontiguously, or in broadly separated spectral allocations [6]–[8]. In addition, multiple-input multiple-output (MIMO) front ends require active antenna elements and arrays with different feeds and separations for carrier frequencies that are spaced far apart (see [9]). In carrier-aggregated MIMO front ends, different carrier frequencies correspond to different antenna array element spacings, requiring multiple antenna elements fed by the same power amplifier (PA). For the dual-band case, a single array with a $\lambda_1/2$ period designed for the lower frequency will result in grating lobes and thus loss of power in unwanted directions at the higher band, while a $\lambda_2/2$ spacing at the higher frequency will result in reduced directivity and increased coupling between antenna elements at the lower frequency. An antenna element for each band is needed to maintain the radiation pattern performance, which implies two loads for the same broadband PA.

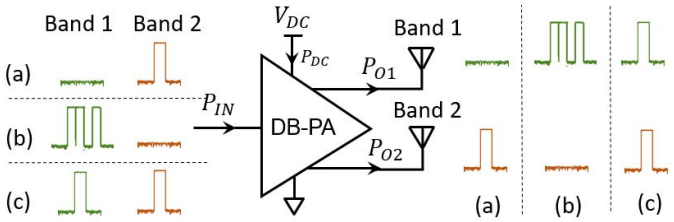

Fig. 1. Block diagram of the dual-band, dual-output PA. Instead of using two separate amplifiers operating at two broadly separated frequencies, the composite input signal is amplified by a single-transistor GaN PA and delivered to two separate antennas. Three transmission scenarios are supported. (a) Nonconcurrent contiguous in a single band. (b) Nonconcurrent noncontiguous in a single band. (c) Concurrent contiguous on two bands.

In this paper, a high-efficiency dual-band PA (DB-PA) with an output diplexer for carrier aggregation is demonstrated. The architecture, shown in the block diagram representation in Fig. 1, targets MIMO arrays by partially performing the function of the dual-array feed networks with its dual-output output matching network (OMN). This paper describes the adaptation and expansion of single-band design techniques for the multifrequency operation, an investigation of signal interaction within the transistor under dual-band concurrent operation, and a method for reducing unwanted mixing. The development of a new algorithm is presented which generates carrier aggregated signals, simulating an arbitrarily shaped multiband signal with a given peak-to-average power ratio (PAPR) and Rayleigh probability density function (pdf) without the reliance on a particular standard. The algorithm can be easily adapted to 5G up- and downlink orthogonal frequency-division multiplexing signals and further generalized for future study of multiband PAs [10].

Manuscript received October 18, 2018; revised December 21, 2018; accepted January 4, 2019. Date of publication February 20, 2019; date of current version July 1, 2019. This work was supported in part by the ONR under Award N00014-17-1-2951, monitored by Dr. P. Maki. The work of Z. Popovic was supported in part by a Lockheed Martin Endowed Professorship and in part by National Instruments for gift and equipment support. This paper is an expanded version from the IEEE MTT-S Radio and Wireless Week Topical Conference on RF/Microwave Power Amplifiers for Radio and Wireless Applications, Anaheim, CA, USA, January 14–17, 2018. *(Corresponding author: Tommaso Cappello.)*

The authors are with the Department of Electrical, Computer, and Energy Engineering, University of Colorado Boulder, Boulder, CO 80309 USA (e-mail: tommaso.cappello@colorado.edu).

Color versions of one or more of the figures in this paper are available online at http://ieeexplore.ieee.org.

Digital Object Identifier 10.1109/TMTT.2019.2895534

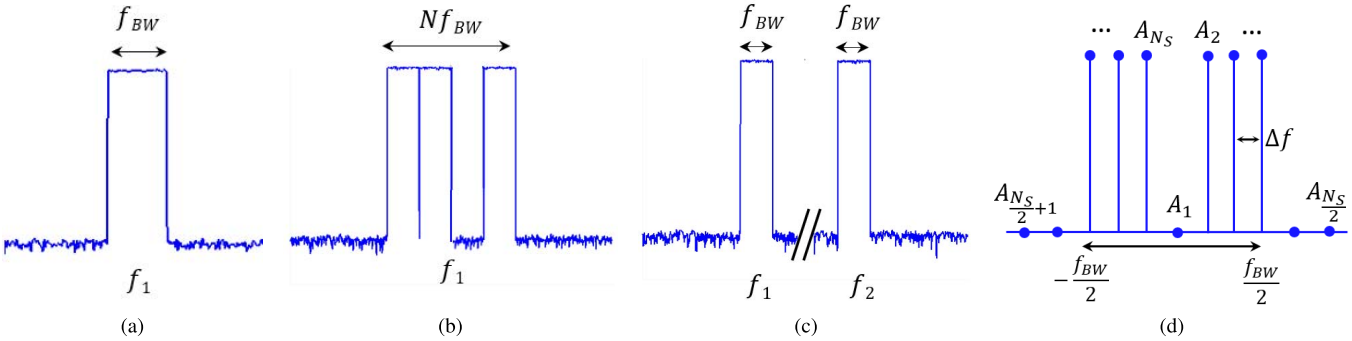

Fig. 2. Different transmission scenarios in carrier aggregation schemes. (a) Contiguous carriers in a single band. (b) Noncontiguous carriers in a single band. (c) Contiguous carriers on different bands. (a)–(c) Spectra are the result of the algorithm initialized with PAPR = 6 dB, $f_S = 100$ MHz, and $f_{\mathrm{BW}} = 20$ MHz. (d) Decomposition of the spectra in a multitone signal; the frequency bins are shaped by setting the amplitudes A_k to obtain the desired spectrum profile.

Existing work in multiband PAs explores the design space along many axes of operating conditions including frequency, class of operation, and load modulation. For example, the harmonic control for modulated signals is investigated in [11] and [12], the incorporation of envelope tracking in [13] and [14], and dynamic load modulation in [15]. This paper extends the approach in [16], which presents a single-input/dual-output OMN for a DB-PA with two separate loads. We apply the design approach from [16] to a complete PA design and characterize the resulting DB-PA for a variety of signals representative of 5G requirements.

Multifrequency operation can be classified as either concurrent or nonconcurrent. The former indicates that a single PA is amplifying multiple bands simultaneously, and the latter indicates a set of single-band PAs operating in parallel with a combiner. Both concurrent [17]–[21] and nonconcurrent operation [11], [22] have been investigated with various technologies, including gallium nitride (GaN) as well as silicon [23], and varying signal bandwidths, from 5 to 20 MHz. The concurrent operation is particularly challenging as it often results in lower efficiency, degraded spectral emissions, and adjacent channel power ratio (ACPR). For example, Rawat and Ghannouchi [24] present a PA where the interaction of the two signals results in faster saturation, lower efficiency, and degraded ACPR. Subsequent work in [25] introduces the intermodulation impedance tuning to reverse engineer this mechanism for the improved efficiency. An example of the concurrent multisignal linearization with closely spaced carriers is shown in [26], where in-band, cross, and inter-band modulation by-products are jointly extracted for dual-band digital predistortion (DPD), resulting in 5-dB improvement in linearity for two 40-MHz LTE signals 40 MHz apart.

From a digital signal processing perspective, there is no difference between contiguous or noncontiguous bands, as discussed in [27]; however, from a PA point of view, these different cases affect both PA design and RF test hardware requirements. As more subcarriers are added to the signal, PAPR may increase up to 10–13 dB, impacting PA efficiency [28]. Therefore, when characterizing PAs for concurrent bands with aggregated signals, it is critical to generate test signals with arbitrary band distributions, PAPRs, and bandwidths.

The signal PAPR in carrier aggregation scenarios is typically controlled by processing the signal in the digital baseband with a crest factor reduction (CFR) algorithm [29], [30]. These algorithms can be based on the clipping and filtering [31], partial transmit sequence [32], or selective mapping [33] techniques. This paper takes an alternative approach and synthesizes an arbitrary signal without reliance on a particular standard. Multitone signals with preselected envelope statistics and modulation bandwidths can be employed to evaluate the PA performance [34]–[38]. In [36], a telecommunication signal is approximated with a multisine sequence by means of an iterative algorithm that conserves the first-order statistics and bandwidth of the original signal. The new algorithm presented in this paper replicates and generates various signal scenarios, including arbitrarily shaped spectral bands.

This paper is organized as follows. In Section II, the algorithm capable of controllable-PAPR signal generation is detailed. Section III describes the design, implementation, and performance of the dual-band, dual-output PA under continuous wave (CW) excitation, with a gain model for DB-PA given in the Appendix. The setup and calibration of a test bench for modulated concurrent signals is presented in Sections IV and V, before the application of DPD to the amplifier under both nonconcurrent and concurrent DB drives in Section VI.

II. Carrier-Aggregated Signal Generation With Arbitrary PAPR

In order to characterize the dual-band, dual-output PA with both nonconcurrent and concurrent signals, a new signal generation algorithm for multiband signals is presented. This algorithm can replicate different spectral scenarios typical of carrier aggregation [6], [7], as summarized in Fig. 2(a)–(c), with arbitrary signal PAPR. Such flexible signal generation enables the comprehensive characterization of PA for a more thorough understanding of the system performance. Whereas conventional methods such as CFR operate on an existing signal to produce a desired PAPR, this algorithm described in this section directly synthesizes a signal with the required statistics.

Consider a discrete-time system in which a signal $x(t)$ of period T and bandwidth f_{BW} is sampled at $f_S > 2f_{\mathrm{BW}}$. This results in a sequence of samples x_k, which can be written in

polar form as

$$x_k = A_k e^{j\phi_k}, \quad k = 1, \ldots, N_S \; N_S = T f_S. \tag{1}$$

If the sequence of symbols x_k is modulated by N_C-independent subcarriers with $N_C = T f_{\mathrm{BW}}$, the resulting multicarrier signal $x(t)$ is given by

$$x(t) = \sum_{k=1}^{N_C} x_k e^{j2\pi k \Delta f t} = \sum_{k=1}^{N_C} A_k e^{j(2\pi k \Delta f t + \phi_k)} \tag{2}$$

where Δf is the frequency spacing between adjacent carriers. Δf corresponds to the fundamental frequency $1/T$ of the sequence. The minimum number of carriers can be estimated by $N_C \geq 1.2\ f_{\mathrm{BW}}/\Delta f$ [39].

PAPR of signal $x(t)$ is defined as the ratio of the peak to the average power over period T

$$\mathrm{PAPR} = \frac{\max |x(t)|^2}{E|x(t)|^2} \xrightarrow{(2)} \mathrm{PAPR}(A_k, \phi_k). \tag{3}$$

As demonstrated analytically in [40], PAPR of the multicarrier sequence (2) depends on the choice of amplitudes A_k and of phases ϕ_k, and a nonlinear relationship exists between the PAPR, the amplitude, and the phase distributions of the N_C subcarriers. Here, we adjust amplitudes A_k of the subcarriers to achieve a preselected spectral shape, while the phases are chosen to impose an arbitrary PAPR upon signal $x(t)$. This is accomplished through an iterative method, such as the Gauss–Newton algorithm [41], and the definition of a least-squares cost function

$$J(\phi_k) = \min |\mathrm{PAPR}(\phi_k) - \mathrm{PAPR}_D|^2 \tag{4}$$

where PAPR_D is the desired PAPR of the sequence. At every iteration, the Gauss–Newton algorithm performs a local linearization of function $\mathrm{PAPR}(\phi_k)$ with respect to the phases ϕ_k and converges quadratically to one of many possible local minima. Therefore, the algorithm requires a proper initialization to converge to a solution.

In [40], a PAPR reduction technique for multicarrier signals is described and parabolic phase shaping suggested for the PAPR control

$$\phi_k = \pi \frac{(k-1)(k-2)}{N_S - 1}. \tag{5}$$

In this paper, (5) is employed to initialize the algorithm for the fast convergence toward arbitrary values of PAPRs and spectral shapes. Fig. 3 shows a possible initialization of the algorithm; the A_k amplitudes of the subcarriers are initialized with a Gaussian white random distribution, whereas phases ϕ_k are shaped as in (5). With this parabolic initialization, the phase of each sinusoidal component is iteratively adjusted by $\Delta\phi_k$, with the ith iteration of the algorithm given by

$$\phi_k^{i+1} = \phi_k^i + \Delta\phi_k^i \tag{6}$$

where $\Delta\phi_k^i$ represents the optimal phase increment in the least-squares sense and can be calculated as [41]

$$\Delta\phi_k^i = (S^T S)^{-1} S^T \Delta\mathrm{PAPR}^i. \tag{7}$$

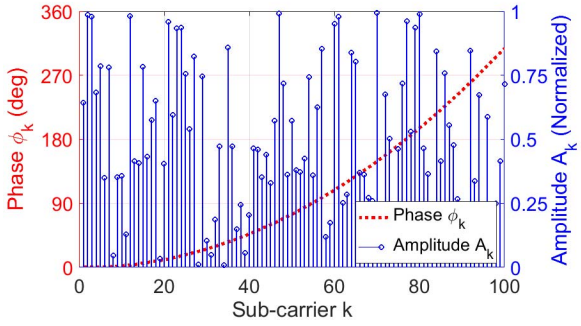

Fig. 3. Possible initialization sequence of the algorithm with random amplitudes and parabolic phase distribution. The sequence is characterized by $f_{\mathrm{BW}} = 10$ MHz bandwidth, $N_C = 100$ subcarriers, $T = 10\ \mu$s period, and a sampling frequency $f_S = 100$ MHz.

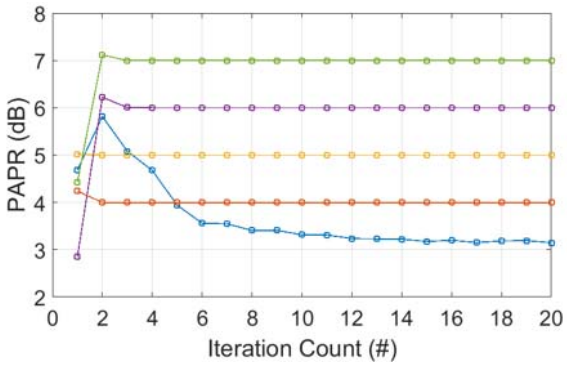

Fig. 4. Convergence of the algorithm for different PAPRs. The sequences are initialized with parabolic phase shaping [40] and with randomized subcarrier amplitudes. The algorithm converges in two-to-three iterations for PAPR > 3.

In (7), $\Delta\mathrm{PAPR}^i = \mathrm{PAPR}^i(\phi_k) - \mathrm{PAPR}_D$ is the output residual while S is the sensitivity array whose elements are the partial derivatives of $\mathrm{PAPR}(A_k, \phi_k)$ with respect to each phase

$$S = \left(\frac{\partial \mathrm{PAPR}^i}{\partial \phi_1^i}, \ldots, \frac{\partial \mathrm{PAPR}^i}{\partial \phi_k^i}, \ldots, \frac{\partial \mathrm{PAPR}^i}{\partial \phi_{N_S}^i} \right). \tag{8}$$

The algorithm can be explained as follows. Fig. 2(a)–(c) shows three target spectral profiles. The amplitudes of the harmonics are controlled by array A_k. For instance, frequency notch Δf can be introduced at the center of the band as shown in Fig. 2(b) by setting $A_1 = 0$. For a broader notch, the array of zeroed amplitudes can be expanded to multiple subcarriers [Fig. 2(c)].

The algorithm is impractical for use in cases of very broad signal spacing (larger than the relative bandwidth of each channel). The complexity of the problem scales quadratically with the number of carriers N_C which is proportional to f_{BW}. To address this problem, we generate a sequence with a given PAPR (e.g., 6 dB) with a single frequency notch at $A_1 = 0$ as qualitatively depicted in Fig. 2(d). The frequency-domain complex samples $\{x_{N_S/2+1}, \ldots, x_{N_S}\}$ are modulated around f_1 and transmitted on the first band, while samples $\{x_2, \ldots, x_{N_S/2}\}$ are modulated around f_2 and transmitted on the second band. With this method, two broadly separated signals can

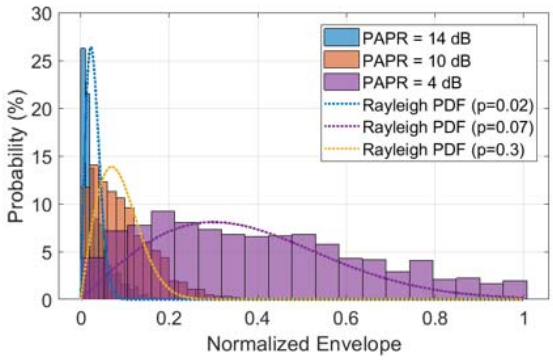

Fig. 5. Envelope histogram of three realizations of sequences generated with the algorithm, with equal bandwidths but different PAPRs (4, 10, and 14 dB). The most likely Rayleigh pdf is fit to bins of each sequence.

be transmitted with a total PAPR controlled by the algorithm. We note that the individual PAPR of the two signals is not controllable by the algorithm.

Fig. 4 shows the convergence of the algorithm for different PAPRs. For high PAPRs, the desired result is achieved in only two-to-three iterations. For PAPRs lower than 4 dB, the algorithm struggles to converge because only the phases are controlled while the amplitudes are constrained by the preselected spectral shape. However, the purpose of this algorithm is the generation of high-PAPR signals such as those found in 5G systems [42], and the slow convergence speed at PAPR<4 dB is not critical. Fig. 5 shows the histogram of the amplitudes of three generated sequences, with the same spectral shaping and different PAPRs. Superposed with the numerical results of the algorithm are Rayleigh pdfs showing good agreement with the numerical simulations.

III. Dual-Band/Dual-Output PA

The DB-PA described in this section demonstrates the feasibility of the dual-output carrier aggregation concept, delivering modulated signals at two frequencies to two independent loads. The DB-PA topology is depicted schematically in Fig. 6. The layout of the 8.7 cm × 6.3 cm prototype is shown in Fig. 7. Following the method detailed in [16], the updated OMN consists of four subcircuits in two separate branches. Each branch is designed to present the target impedance within its band, while behaving as an open circuit in the other band. This reduces the loading effects between the two branches and prevents the signal transmission outside of the design frequencies of the two bands, as is experimentally verified in Section VI.

While the method applies generally, in this case, the 3.5-GHz WiMAX and 5.8-GHz ISM bands are chosen as initial carrier frequencies. Load–pull simulations are performed using Keysight ADS and the manufacturer-provided nonlinear transistor model at two operating frequencies, $f_1 = 3.5$ GHz and $f_2 = 5.8$ GHz. Simulated load–pull contours, taken at the Z_{LP} planes at the two design frequencies, are shown in Fig. 8. For this single-tone (nonconcurrent) scenario, the point of optimal power-added efficiency (PAE) is found for fundamental load impedances of $(14.4 + j2.7)\ \Omega$ at f_1 and $(26.8 - j62)\ \Omega$ at f_2. No harmonic termination is done in the design. The simulated impedances at the Z_{LP} reference plane at $2f_1$, $3f_1$, $2f_2$, and $3f_2$ are given in Table I. Note that exciting the transistor with a DB signal would yield a slightly different set of target load–pull impedances for PAE and output power in both bands. Because the presented PA is intended for use in both concurrent and nonconcurrent operating modes, only one mode can be optimized for. Here, separate single-frequency load–pull simulations are found to be the most appropriate ones for design. Certainly, the simulation complexity and expected accuracy of load–pull simulations are expected to be higher for the single-tone condition. This design choice is validated by the measurements in Section VI.

With the target load impedances determined, transformations are performed to match the desired impedances to the output-port 50-Ω loads. Starting from the two output ports and moving back toward the transistor drain, a real-to-real transformation is first performed on both 50-Ω loads to "intermediate" impedances ($R_{\mathrm{LP},1}$ and $R_{\mathrm{LP},2}$). This real-to-real transformation is a Chebyshev network created following tables in [43]. Real-to-complex transformations then present the desired load–pull complex impedances ($Z_{\mathrm{LP},1}$ and $Z_{\mathrm{LP},2}$) at the reference plane after the bias network and tee-junction (see Fig. 6) at the two frequencies of interest. The tee-junction reference planes are defined where each band presents an approximate RF open at the other frequency band of interest; at the $Z_{\mathrm{LP},1}$ plane, the network is simulated to present at f_2 an impedance of $(11 + j207)\ \Omega$. At the $Z_{\mathrm{LP},2}$ plane, the network presents at f_1 an impedance of $(163 + j1010)\ \Omega$. The simultaneous dual-band match-open design between f_1 and f_2 is determined through an iterative process of tuning the magnitude of the near-open circuit presented at one frequency while revising the PAE match at the second frequency.

The design of the DB-PA is performed with a Wolfspeed-Cree 6-W CGH40006P packaged GaN transistor on a 30-mil Rogers 4350B substrate. A quiescent point in the deep class-AB region is selected, with $V_{\mathrm{DS}} = 28$ V and $I_{\mathrm{DS}} = 40.8$ mA. A parallel RC circuit (ATC600S 2 pF, KOA0402 50 Ω) at the gate, along with a 100 Ω resistor in the gate bias line, is added for stabilization. Because $f_2 = 5.8$ GHz approaches the upper limit of this transistor's frequency range, resulting in a drop in gain at the higher band, load–pull simulations are performed with a 28-dBm input drive, 2 dB higher than at the lower band.

As described in [16], a stub-tuned design was chosen to implement both of the real-to-complex transformation subcircuits. This approach uses resonant networks to produce "loops" in the Smith chart to match the desired impedance, as shown in Fig. 8(c), where the simulated input reflection of the dual-band matching network from [16] is plotted across the two frequencies of interest and compared to the simulated load–pull contours. Lumped-element capacitors (ATC600S) were used in [16] to reduce circuit size, but these degrade the amplifier efficiency due to their lower Q (<100 at the upper operating frequency). By removing these lumped elements and using 500S capacitors in the bias tee, the insertion loss (IL) and its impact on PAE are reduced.

The OMN of the amplifier presented in this paper is a new iteration using exclusively low-loss microstrip lines and

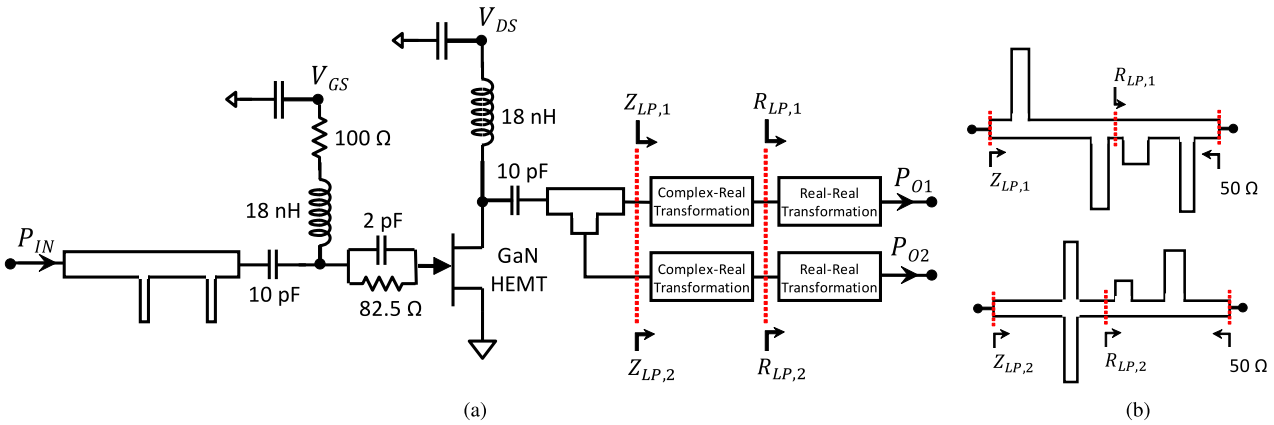

Fig. 6. Block diagram of the dual-band, dual-output PA. (a) The dual-band input matching network is designed from simulated source–pull and includes an *RC* stability network. (b) Details of the layout topology of the OMNs (dimensions not to scale) with corresponding reference planes of the transformed impedances.

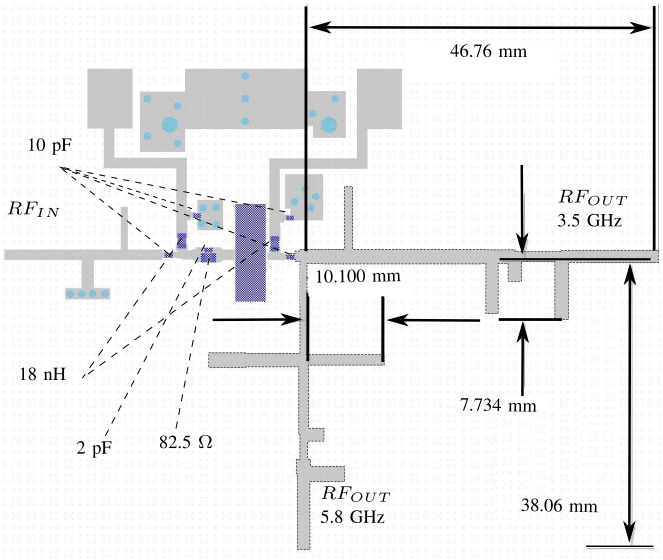

Fig. 7. Layout of the output network, including dimensional guidelines for the matching stub networks and the transistor and lumped element placements depicted in blue.

omitting lossy lumped elements. The simulated return loss and IL for each path of the three-port OMN are shown in Fig. 9. The simulated return loss of each path is 19.5 and 4.3 dB at $f_1 = 3.5$ GHz and $f_2 = 5.8$ GHz, respectively, with IL of 0.3 and 0.6 dB. Insertion loss is here defined as $\text{IL} = 10\log_{10}(|S_{21}|^2/(1-|S_{11}|^2))$ and takes into account the impedance mismatches. The relatively low magnitude return loss is a result of a tradeoff in design between reducing IL and improving return loss.

Fig. 10 shows the measured PAE, delivered power, and gain under CW, single-band excitation across frequency. A flat output power within each band is measured, with slightly higher output power at the upper band due to the higher input drive. Measured efficiency is a few points lower than the simulated value, and the gain is 2 dB lower, with narrower bandwidth at the lower band. This discrepancy is attributed to a combination of fabrication inaccuracy and device deviation

TABLE I
IMPEDANCE PRESENTED BY EACH BRANCH AT SECOND AND THIRD HARMONICS

	$2f_1$ (7 GHz)	$3f_1$ (10.5 GHz)	$2f_2$ (11.6 GHz)	$3f_2$ (17.4 GHz)
$Z_{LP,1}$	$39-81j$	$38+35j$	$29-10j$	$176-19j$
$Z_{LP,2}$	$6+24j$	$168+768j$	$2-84j$	$16-81j$

from the large-signal model. The maximum PAE is measured at 3.4 and 5.5 GHz, which are both within 5% of the design frequencies. In the upper band, the shift is likely due to fabrication tolerances and can be mitigated with more exact circuit-printing methods. Thus, for all subsequent measurements of the amplifier presented in this paper, the upper operating frequency is 5.5 GHz. Table II summarizes the simulated and measured results of each band characterized individually at maximum PAE.

IV. EXPERIMENTAL SETUP

An experimental setup based on two National Instruments vector signal transceivers (VSTs) is used to characterize and linearize the DB-PA with multiband signals. A block diagram and a photograph of the experimental setup are shown in Fig. 11. The two VSTs are programed to generate complex modulated signals $x_1(t)$ and $x_2(t)$ at $f_1 = 3.5$ GHz and $f_2 = 5.5$ GHz, respectively. VST 1 is a PXIe-5646R with 200-MHz instantaneous bandwidth, while VST 2 is a PXIe-5645R with 80 MHz. Each VST contains a 16-bit vector signal generator (VSG) and a 16-bit vector signal analyzer (VSA), with an internal local oscillator and upconverter to provide the frequency shift at the carrier frequencies f_1 and f_2. The setup is controlled via LabVIEW. Input and output calibration parameters are automatically de-embedded by the software, and time-alignment constants are extracted during the calibration of the setup.

The two VSTs are precisely synchronized to enable the predictable generation and acquisition of signals. The local oscillators of VSG 1 and VSA 1 are phase locked, as are

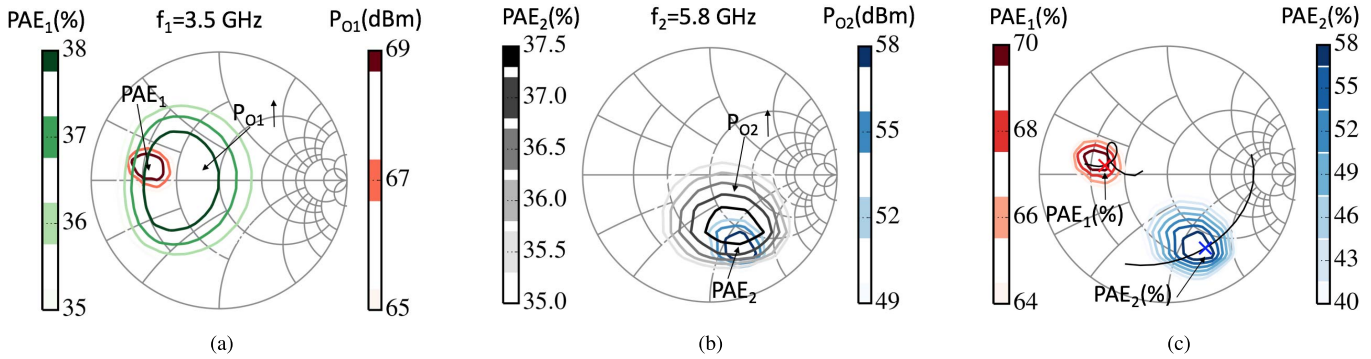

Fig. 8. Simulated single-tone load–pull contours, taken at the Z_{LP} plane (see Fig. 6) of the CGH40006P device biased at $V_{DS} = 28$ V and $I_{DS} = 40.8$ mA. Output power and PAE contours are shown for two nonconcurrent input tones of (a) $P_{IN1} = 26$ dBm at 3.5 GHz and (b) $P_{IN2} = 28$ dBm at 5.8 GHz. (c) Input reflection ($|S_{11}|$ parameter) of the previous iteration of OMN fabricated in [16] is plotted across the two frequency bands of interest, with the response at 3.5 and 5.8 GHz marked accordingly.

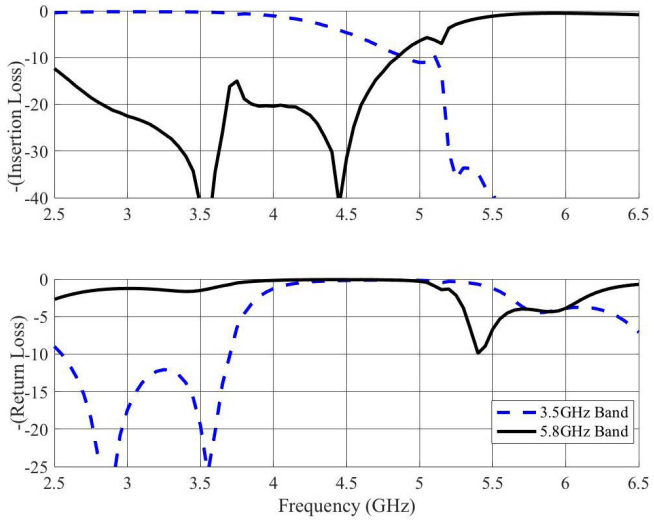

Fig. 9. Simulated negative IL and return loss of the three-port network for f_1 (dashed) and f_2 (solid), under single-band, nonconcurrent excitation. The designed network provides the isolation greater than 40 dB between bands.

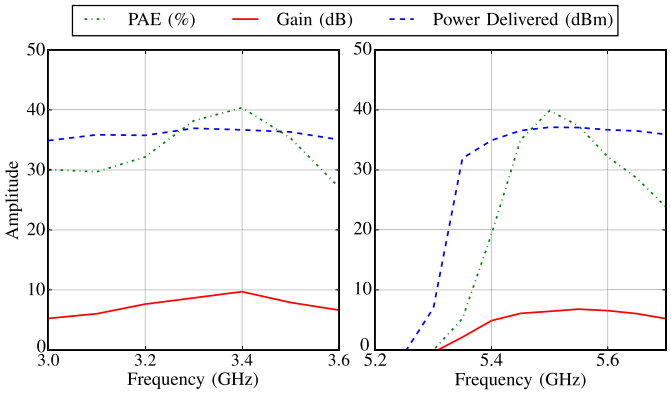

Fig. 10. Measured CW PAE, gain, and output power over the two bands. Peak PAE and output power are observed around 5.5 GHz.

those of VSG 2 and VSA 2. The two VSTs are mounted in a PXI-express rack and share the same 10-MHz clock reference. The generation and acquisition of the two signals are performed with a master–slave triggering architecture. The generation of $x_1(t)$ and $x_2(t)$ is synchronized with a hardware trigger generated by VST 1, and the sampling of the two outputs of PA, $y_1(t)$ and $y_2(t)$, are activated by the same trigger.

The outputs of the two VSTs are combined with a resistive combiner (Keysight 11667B) and the resulting signal amplified by a bench-top driver amplifier (Mini-Circuits ZVE-3W-83+). The output of the driver is calibrated for amplification up to 28 dBm at 3.5 and 5.5 GHz. A high-pass output filter (Mini-Circuits ZX75HP-2400-S+) is used to attenuate the significant intermodulation products at $5.5 - 3.5 = 2$ GHz and $|3.5 - 5.5| = 2$ GHz generated by the driver.

Precise time alignment is required between all the four signals in the setup $\{x_1(t), x_2(t), y_1(t), y_2(t)\}$. Three constant time delays are obtained during the calibration from small-signal measurements. First, the delay time between $x_1(t)$ and $y_1(t)$ is evaluated with the other channel turned off ($x_2(t) = 0$). Similarly, the delay between $x_2(t)$ and $y_2(t)$ is extracted with the other channel disabled. The difference between these two delays is largely due to different models of VSTs. Finally, the cross-delay between the two channels is extracted. To verify the accuracy of this alignment process, a cross correlation of the signal envelopes is done in post-processing.

The linearity of the setup is verified with a two-tone test and a spectrum analyzer (VST PXIe-5840) connected at the input reference plane P_{IN} of DUT. The results are shown in Fig. 12(a) which demonstrates a spurious-free dynamic range (SFDR) up to 40 dB for a 28-dBm CW tone at both operating frequencies. While the setup is unable to discriminate between the nonlinearities generated by the driver amplifier and that of PA, the two-tone test indicates that the most significant nonlinearity is introduced by PA, and therefore DPD can linearize the overall driver-PA chain. The linearity of the setup is also verified with modulated signals in the two bands of interest, and the resulting spectra are reported in Fig. 12(b) and (c).

With the setup verified in terms of the large-signal linearity, power calibration is performed in each band individually.

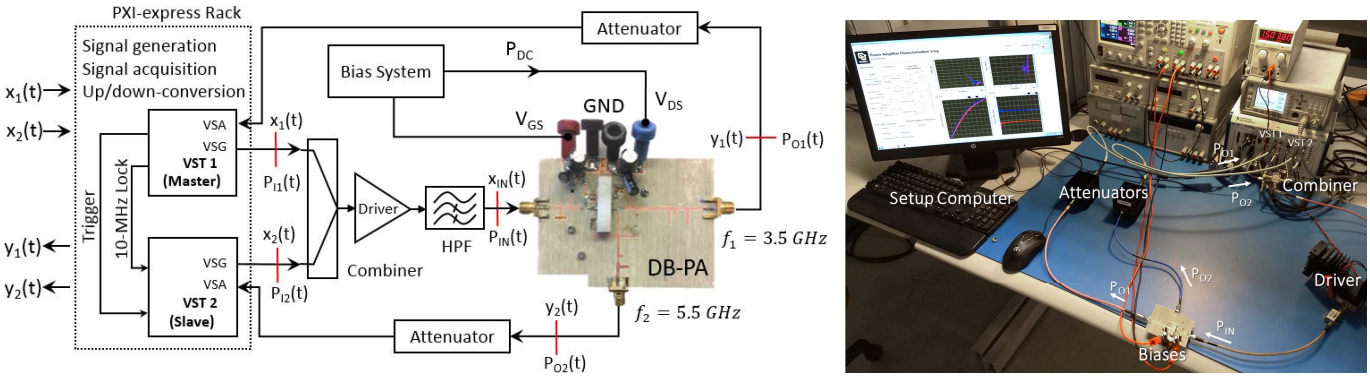

(a) (b)

Fig. 11. Experimental setup for the test of the dual band, dual-output PA with the concurrent signal generation and analysis. (a) Block diagram of the setup. Two NI VSTs are synchronized at baseband by means of 10-MHz lock and a hardware trigger. The outputs of the two VSTs are power-combined and amplified by a bench-top driver. A high-pass filter rejects the intermodulation products at low frequency. The PA is a single transistor with dual-band and dual-output OMN. The two outputs are attenuated separately and acquired by the setup. (b) Photograph of the setup.

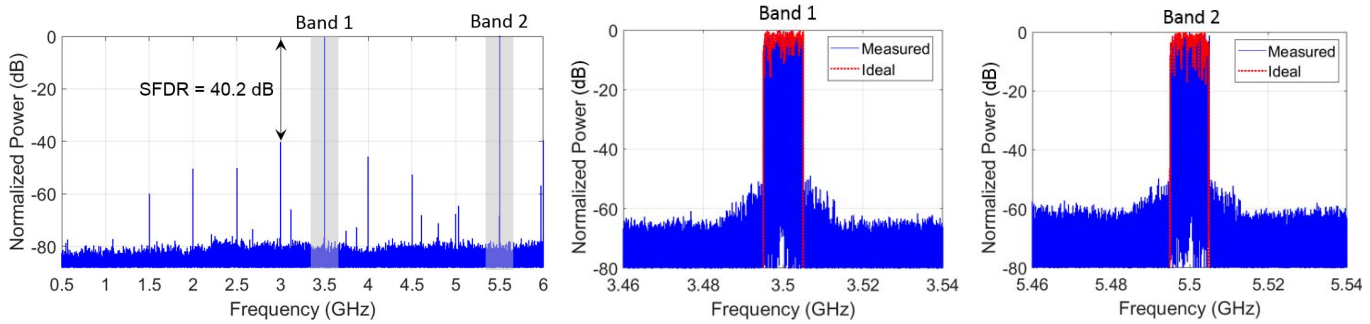

(a) (b) (c)

Fig. 12. Significant spectra of the DUT input signal generated by the setup. (a) Broadband spectrum acquisition of a two-tone signal with 28-dBm power each and 2-GHz spacing, SFDR of the calibrated setup is over 40 dB. (b) and (c) Narrowband acquisition around the two carriers for two concurrent signals with 10-MHz bandwidth and 6-dB PAPR.

TABLE II
CW PERFORMANCE OF THE FABRICATED DUAL-BAND PA

	Lower Band		Upper Band	
	Sim. (3.5)	Meas. (3.4)	Sim. (5.8)	Meas. (5.5)
PAE	46.0%	40.4%	43.3%	39.9%
Output Power	37.3 dBm	36.7 dBm	37.5 dBm	37.1 dBm
Gain	11.3 dB	9.7 dB	8.6 dB	6.4 dB
Gain BW (-1 dB)	7.0%	4.4%	4.3%	4.5%

A single tone is first generated in the lower band with VST 1, and the RF power at the DUT reference plane P_{IN} is measured with a power meter. Subsequently, the upper band is calibrated in a similar fashion. To measure the output attenuations, an RF source (Keysight 83650A) generates spectrally clean input tones, first at f_1 and then at f_2. These two signals are injected at the two output reference planes P_{O1} and P_{O2} of DUT. The attenuation values before and after the receiver chains are measured and result in 30.6 dB for f_1 and 31.4 dB for f_2.

V. PA CHARACTERIZATION FOR DUAL-BAND OPERATION

For this dual-output design, the two bands can be linearized independently about their center frequencies in the nonconcurrent operation. If the amplifier instead had only a single output, the application of DPD would require a wide bandwidth covering the entire frequency span. For concurrent operation, however, a theoretical framework is needed to describe the PA gain under the concurrent operation. The DB-PA gain model developed for this characterization is described in detail in the Appendix and used in this section to characterize the DB-PA under nonconcurrent and concurrent operations.

A. Characterization in Nonconcurrent Mode

In this characterization, DB-PA is alternately stimulated with a pulsed signal modulated at $f_1 = 3.5$ GHz and $f_2 = 5.5$ GHz. A Gaussian amplitude-modulated pulse of 10-μs duration and 100-μs period is employed as in [44] while the other channel is disabled. This single-frequency characterization enables the evaluation of the gains, $|G_{11}|$ and $|G_{22}|$, and of the cross-gains, $|G_{12}|$ and $|G_{21}|$ (see Appendix).

The results of this characterization are provided in Fig. 13 for the two bands of interest. When a pulsed input signal centered at f_1 is amplified by DB-PA, the power gain $|G_{11}(P_{I1}, 0)|$ is approximately 10 dB, whereas the cross-gain at the other port is $|G_{21}(P_{I1}, 0)| \approx -27$ dB. For the other carrier, the power gain $|G_{22}(0, P_{I2})|$ is approximately 9 dB while the cross-gain results in $|G_{12}(0, P_{I2})| \approx -26$ dB. These low cross-gain values result in low RF power leakage between opposite ports and are the result of the diplexer-like OMN design discussed in Section II.

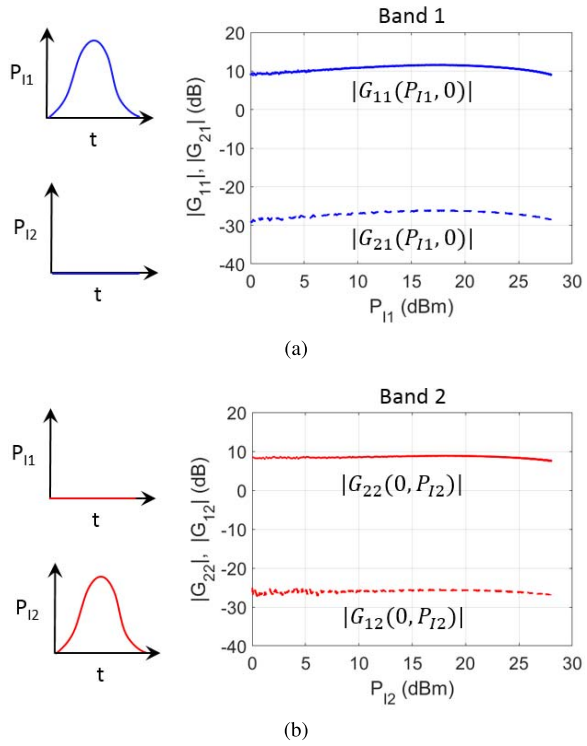

Fig. 13. Measured gains in the nonconcurrent mode (single signal). (a) Gain $|G_{11}|$ and cross-gain $|G_{21}|$ at 3.5 GHz. (b) Gain $|G_{22}|$ and cross-gain $|G_{12}|$ at 5.5 GHz. The low cross-gain values are enabled by the presented matching network.

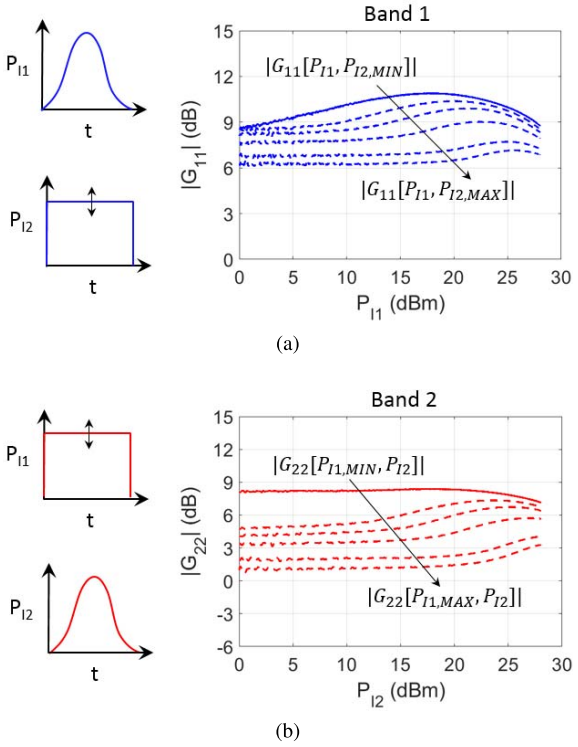

Fig. 14. Measured gains in the concurrent mode (two signals superposed). (a) Gain variation of $|G_{11}|$ at discretized power levels $P_{I2} = \{-\infty, 18, 21, 24, 27, 28\}$ dBm. (b) Gain variation of $|G_{22}|$ at discretized power levels $P_{I1} = \{-\infty, 18, 21, 24, 27, 28\}$ dBm.

B. Characterization in Concurrent Mode

The DB-PA is next tested with two concurrent signals in the two bands of interest. An AM pulse with the Gaussian shaping is synchronously injected into the amplifier together with a rectangular pulse. Both signals have 10-μs duration and 100-μs period. In this characterization, we employ the gain model formulated by (13) (see Appendix).

Fig. 14 shows how the gain in each band varies as the input power in the opposite band increases. The superimposed signal in the opposite band is swept from a small-signal level up to the maximum value (i.e., $P_{Ii,\mathrm{MAX}} = 28$ dBm). As the input power increases, the gain of the DB-PA reduces significantly with about 4–5 dB of variation. This could be due to the faster saturation of the PA as hypothesized in [24] or perhaps a shift in the target impedances.

Fig. 15 shows the variation of the DB-PA gain in compression due to the cross-modulation between the two bands. In this plot, we can identify three regions. The central region corresponds to the small-signal operation, in which both input signals are low enough (i.e., $P_{Ii} < 18$ dBm) and do not affect each other. In this region, the DB-PA behaves linearly and a 1-D DPD can be used separately in both channels, largely for AM/phase modulation (PM) corrections. In the two other regions (i.e., $-18 < P_{Ii} < 28$ dBm) on either side, the gain of DB-PA at peak compression is affected by the second signal. Predistortion must take into account both signals (e.g., using a 2-D memory polynomial).

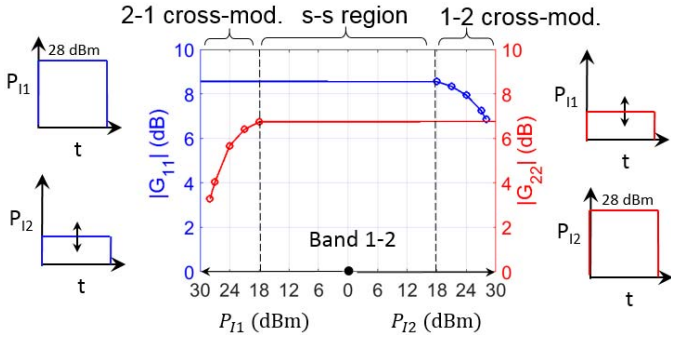

Fig. 15. Measured gain at maximum output power for f_1 and f_2. Significant gain variation due to the cross-modulation is evident. $|G_{11}|$ gain variation when $P_{I1} = 28$ dBm and $P_{I2} = \{-\infty, 18, 21, 24, 27, 28\}$ dBm (left). $|G_{22}|$ gain variation when $P_{I2} = 28$ dBm and $P_{I1} = \{-\infty, 18, 21, 24, 27, 28\}$ dBm (right).

VI. Experimental Results

This section presents the results and a performance summary of DB-PA operated in three different carrier-aggregation scenarios shown in Fig. 2: independent, nonconcurrent amplification of two contiguous and noncontiguous signals in each band, and operation with concurrent signals in the two bands.

For a fair comparison for the PA operation with different inputs, the algorithm is used to generate sequences with a fixed PAPR of 6 dB for all measurements. The DB-PA is biased in the deep class-AB mode with $I_{\mathrm{DS}} = 41$ mA and $V_{\mathrm{DS}} = 28$ V, with a 28-dBm peak power input defined for both bands. A 50-

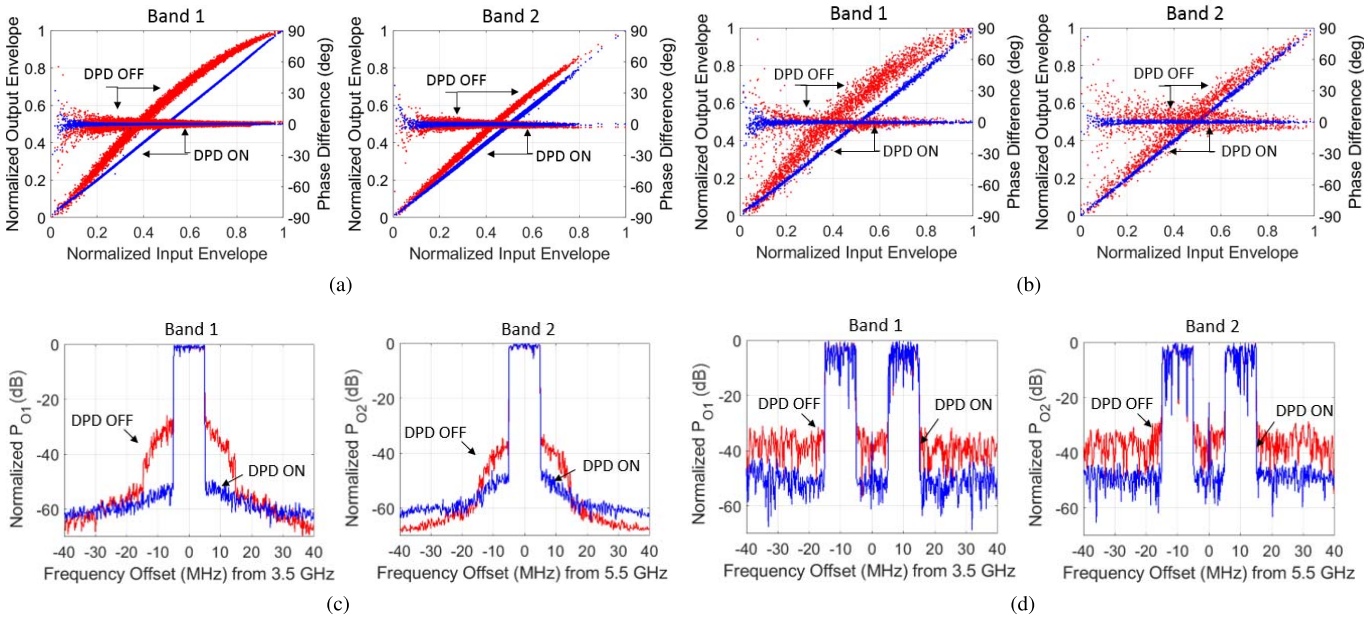

Fig. 16. AM/AM and AM/PM distortion characteristics and relative output spectra, with and without DPD, of the PA operated nonconcurrently in the lower and higher bands. (a) and (c) Response of the DB-PA to a 10-MHz contiguous spectrum. (b) and (d) Response of the DB-PA to a 30-MHz noncontiguous spectrum (10-MHz frequency notch in the middle).

μs sequence is generated with the algorithm which results in 12 500 samples for VST 1 and 6000 samples for VST 2. The output sequence is averaged 16 times to reduce the noise level. An indirect learning approach is adopted for DPD, and no iteration on the coefficient extraction is performed. The postinverse coefficients of the DPD are obtained by means of a conventional least-square algorithm. ACPR and normalized mean square error (NMSE) are used to evaluate the performance of the linearized DB-PA.

A. Nonconcurrent Single- and Dual-Band Operations

The first test is performed with the DB-PA operated in the single-band mode at each frequency with a 10-MHz, 6-dB PAPR signal. A generalized memory polynomial DPD [45] is used to predistort the input signal. For the lower band, a nonlinearity order of 7, a memory order of 3, and no cross-terms are selected, with 17 total coefficients. For the upper band, the number of cross-terms is 3, and the resulting number of coefficients is 89, with the remaining parameters unchanged.

The AM/AM and AM/PM characteristics of the DB-PA at the two bands are shown in Fig. 16(a) with and without DPD. The profile of the upper frequency band shows more distortion than the lower frequency, even with DPD enabled. The output spectra, with and without DPD, are shown in Fig. 16(c). In Fig. 16(c), the lower band shows better spectral purity compared to that of the higher band. This is most likely due to a misalignment error occurring during the extraction of the AM/AM and AM/PM characteristics. As reported in Table II, with 6-dB PAPR and narrowband DPD applied, the amplifier reaches average efficiencies of 29.6% and 19.7% at 3.5 and 5.5 GHz, respectively, when operating nonconcurrently with contiguous signals.

The second test is performed with two signals modulated around each carrier and amplified nonconcurrently by the DB-PA. These two signals are generated with the algorithm with a total PAPR of 6 dB, a relative bandwidth $f_{\mathrm{BW}} = 30$ MHz, and a central frequency notch of 10 MHz. Given the nonconcurrent transmission scenario, a monodimensional DPD, i.e., the generalized memory polynomial [45], is employed. In this test, the DPD algorithm is initialized for both bands with a polynomial order of 7, memory order of 5, and no cross-terms. The AM/AM and AM/PM characteristics of this transmission scenario are shown in Fig. 16(b). Compared to the characteristics of Fig. 16(a), the nonlinear distortion of the DB-PA is higher, most likely due to the higher total bandwidth of the signal (30 MHz versus 10 MHz).

Similar observations and conclusions can be applied to the spectral domain plot shown in Fig. 16(d). DPD is effective in reducing the nonlinear distortion by about 15 dB in the considered frequency range, apart for a single tone at the center of the spectrum that is possibly caused by I/Q unbalance. Table III summarizes the linearity and efficiency performance for both non-contiguous and contiguous signals; the non-contiguous signal test achieves average PAEs comparable to that of the contiguous test, as expected due to comparable PAPRs and pdfs. However, linearity performance, in terms of NMSE and ACPR, degrades for noncontiguous signals.

B. Concurrent Dual-Band Operation

Next, the behavior of the DB-PA under concurrent signal operation is characterized. The two signals, each with 10-MHz bandwidth and a total PAPR of 6 dB, are generated simultaneously by VSTs and injected into the DB-PA. The outputs of the DB-PA are sampled by the setup and time-aligned with the procedure reported in Section IV. For this test, a 2-D

TABLE III
PERFORMANCE SUMMARY OF THE DB-PA

Active Band (i)	Bandwidth (MHz)	PAPR (dB)	NMSE (%)	ACPR (dBc)	Gain (dB)	$P_{Ii,AVG}$ (W)	$P_{Oi,AVG}$ (W)	PAE_{AVG} (%)
Non-Concurrent Single-Band Operation								
1	10	6	0.8	-54.9	11.4	0.10	1.39	29.6
2	10	6	1.3	-51.1	9.0	0.09	0.70	19.7
Non-Concurrent Dual-Band Operation								
1	30*	6	2.5	-52.1	11.4	0.09	1.22	29.0
2	30*	6	1.9	-50.3	8.4	0.13	0.90	22.0
Concurrent Dual-Band Operation								
1+2	–	6	–	–	–	0.25	1.45	25.6
1	10	7.9	2.4	-47	8.2	0.12	0.8	–
2	10	7.6	1.0	-40	7.0	0.13	0.65	–

* 10-MHz frequency notch at the center of the band.

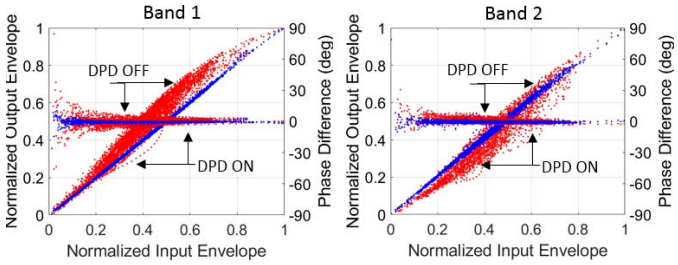

Fig. 17. AM/AM and AM/PM distortion characteristics, with and without DPD, of the PA operated concurrently in the lower band (left) and higher band (right). The signal has 10-MHz bandwidth and 6-dB PAPR.

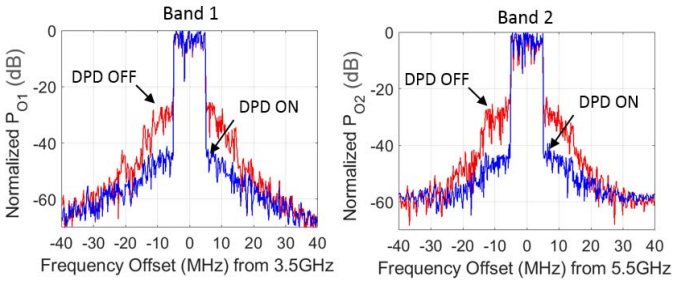

Fig. 18. Output spectra, with and without DPD, of the PA operated concurrently in the lower band (left) and higher band (right). The band is occupied with a 10-MHz 6-dB PAPR contiguous spectrum.

memory polynomial model [46], as in (11), is implemented. An indirect learning architecture is employed for the extraction of the DPD coefficients. A nonlinearity order of 7 and memory order of 1 are considered. When DPD is applied to the concurrent mode, the DB-PA has an NMSE of 2.4%/1.0% and ACPR of −46.8/−48.0 dBc, respectively, in the two bands. The average output power is 0.8/0.65 W, with 4.92 W of dc power consumed for a total PAE of 25.6%. Because of the fixed PAPR in all measurements, the PAE in the concurrent case falls between the two extremes shown in Table II, with the exact values depending on the output power level. The DB-PA performance under concurrent dual-band operation is summarized in Table III, in which the performance is shown both for the overall signal and broken out into the two individual bands (under the concurrent operation). As can be seen, while the signal generation algorithm precisely controls the total signal PAPR, the PAPRs of the two bands considered independently are not controlled to a particular value.

The results of the concurrent dual-band operation are reported in Fig. 17. Significant distortion caused by the cross-modulation within the device is evident from the AM/AM and AM/PM plots which are not present in the corresponding case of a nonconcurrent 10-MHz signal [see Fig. 16(a)]. DPD is nonetheless capable of improving the linearity of DB-PA in the concurrent mode. The resulting spectra, with and without DPD, are shown in Fig. 18.

Fig. 19 displays a broadband acquisition of the two outputs of the DB-PA performed with the VSTs (maximum

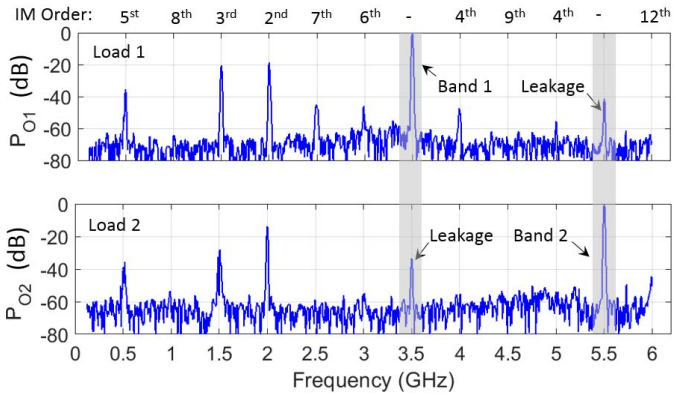

Fig. 19. Broadband spectra of two outputs of the DB-PA operated with two concurrent signals. (P_{Oi} are normalized to the peak value of 36.1 dBm at f_1 and 34.7 dBm at f_2). The DB-PA is capable of amplifying two concurrent signals with low leakage on the other load (−35.8 dBm at f_1 and −41.3 dBm at f_2).

frequency range 0.065–6 GHz). The output powers at f_1 and f_2 are normalized to 0 dBm in order to highlight the dynamic range of the spurs. Power leakage is present on the opposite output of $f_1 = 3.5$ GHz and $f_2 = 5.5$ GHz but is significantly attenuated by the OMN of DB-PA, resulting in the −41.3-dBm leakage at load 1 and −35.8-dBm leakage at load 2. At these two frequencies, no intermodulation products fall in the two bands of the amplifier, and only leakage power is present. The two most significant spurs generated by the

TABLE IV
COMPARISON WITH PUBLISHED DUAL-BAND PAS IN CONCURRENT MODE

Ref.	Architecture	Freq. (GHz)	Bandwidth (MHz)	PAPR (dB)	η_D (%)	PAE_{AVG} (%)	$P_{O,AVG}$ (dBm)	ACPR (dBc)
[17]	Doherty	2.25/3.25	20/20	9.5	34.8	–	37.1	-46/-45.3
[18]	Doherty	1.9/2.6	10/10	7	50.1	45.8	36.82/36.83	-45.1/-44.5, -46.9/-46.4
[19]	Doherty	1.8/2.4	5/10	7	–	35.6	33.2	-46.3/-47.9, -49.4/-47.7
[20]	Doherty	.85/2.33	10/15	7.5	26.7	–	31.75	-47.3/-47.1, -49.4/-49.4
[21]	Single-ended multi-mode	2/2.3	–	9	34.3	–	30.3/30.9	-46.7/-46.1
This Work	**DB-PA single-ended dual-output**	**3.5/5.5**	**10/10**	**6**	**29.5**	**25.6**	**29.03/28.13**	**-46.8/-48.0**

amplifier when operated in the concurrent mode appear at 2 and 1.5 GHz, corresponding, respectively, to the second- and third-order intermodulation products. (The fundamental frequency is 500 MHz.) Considering the frequency spacing of the carriers, these mixing products can be easily attenuated by a filter or by the inherent match of the antenna connected to the output of the DB-PA.

Table IV displays the results of this paper alongside other recent studies in dual-band concurrent operation with modulated signals and DPD, although this DB-PA is not necessarily directly comparable to these works due to its unique dual-output nature, higher frequencies of operation, and lower power level of this single-ended PA (when compared to Doherty PAs) [17]–[20]. The DB-PA operates over the widest noncontiguous absolute bandwidth (2 GHz) compared to the other published results and exhibits comparable ACPR after linearization. The class-AB DB-PA provides a proof-of-concept demonstration of diplexer-like, dual-output carrier aggregation which can be extended to more complex PA architectures.

VII. CONCLUSION

This paper presents a dual-output, dual-band RF PA for the concurrent amplification of signals in two broadly separated sub-6-GHz 5G bands, centered at 3.5 and 5.5 GHz. This amplifier is designed with a diplexer-like OMN that presents an impedance match or a near-open reflection at each frequency on each branch in order to separate two bands into two loads. The DB-PA operates efficiently with carrier-aggregated signals, in which different configurations of bands are present. A new algorithm for the generation of contiguous and noncontiguous spectra with arbitrary PAPRs and Rayleigh pdfs is presented and used to investigate the performance of the DB-PA in different modes of operation. An experimental setup with two synchronized vector signal sources and analyzers is presented and used to generate two signals with 2-GHz carrier separation. A simplified 2-D model of the DB-PA is developed for the characterization over two bands for both nonconcurrent and concurrent operations and given in the Appendix. The quantitative measurement of how concurrent signals of varying power affect gain in each band is presented and discussed. When the PA is used in the nonconcurrent mode, it achieves a gain of 10 dB at 3.5 GHz and 9 dB at 5.5 GHz. A gain variation of 4–5 dB in compression due to cross-modulation is observed when two signals are amplified concurrently.

The presented DB-PA is tested in different transmission scenarios expected in 5G up- and downlinks: with nonconcurrent amplification of contiguous and noncontiguous signals. Low leakage power is measured in the opposite port loads, thereby verifying the diplexer function of the DB-PA in the nonconcurrent operation. In concurrent operation, unavoidable second- and third-order intermodulation products are observed at 2 and 1.5 GHz. These can be reduced in practical applications through filtering, or through the use of narrowband matched antennas. The class-AB DB-PA presented in this paper is a demonstration of an efficient dual-output DB amplifier with carrier aggregation, and the concept can be extended to more complex PA architectures.

APPENDIX

A 2-D polynomial model is assumed for the amplifier, in which the amplitudes of two input signals are the only cause of nonlinear distortion and the relative phase is not relevant [46]. This allows for a simplified study of the characteristics of the DB-PA by considering only 2-D versus 4-D required if phases are taken into account. This hypothesis is later verified by using the 2-D memory polynomial model of the DB-PA for predistortion.

Given the two separate output signals, y_1 and y_2, and the single input, x_{IN}, a general relationship for the gain of the DB-PA can be defined as

$$\begin{bmatrix} y_1 \\ y_2 \end{bmatrix} = \begin{bmatrix} \hat{G}_1(x_{\text{IN}}) & 0 \\ 0 & \hat{G}_2(x_{\text{IN}}) \end{bmatrix} \begin{bmatrix} x_{\text{IN}} \\ x_{\text{IN}} \end{bmatrix} \tag{9}$$

where $\hat{G}_i$ represents the normalized complex gain of PA with respect to the single input and two output ports. As shown in the block diagram of Fig. 11(a), the DB-PA input signal x_{IN} is a function of x_1 and x_2. However, we can assume that the two signals, x_1 and x_2, are linearly combined and amplified around the two bands of interest, as discussed in Section IV. Therefore, it is possible to de-embed the input gain stage of the setup and consider x_1 and x_2 as two separate signals at the DB-PA input reference plane. Gain $\hat{G}_1$ can be split into two gains $\hat{G}_{11}$ and $\hat{G}_{12}$, which are the gains from input x_1 to output y_1 and from input x_1 to output y_2, respectively. Similarly, we can

split Gain $\hat{G}_2$ into two gains $\hat{G}_{22}$ and $\hat{G}_{21}$. Given the input signal separation, (9) can be rewritten as

$$\begin{bmatrix} y_1 \\ y_2 \end{bmatrix} = \begin{bmatrix} \hat{G}_{11}(x_1, x_2) & \hat{G}_{12}(x_1, x_2) \\ \hat{G}_{21}(x_1, x_2) & \hat{G}_{22}(x_1, x_2) \end{bmatrix} \begin{bmatrix} x_1 \\ x_2 \end{bmatrix}. \quad (10)$$

Let us assume a model structure for gain $\hat{G}_{ij}$ of the DB-PA based on the dual-band extension of the memory polynomial [46]

$$\begin{aligned} y_1(n) &= \sum_{m=0}^{M} \sum_{i=0}^{K} \sum_{j=0}^{i} c_{1,mij} x_1(n-m) \\ &\quad \times |x_1(n-m)|^{i-j} |x_2(n-m)|^j \\ y_2(n) &= \sum_{m=0}^{M} \sum_{i=0}^{K} \sum_{j=0}^{i} c_{2,mij} x_2(n-m) \\ &\quad \times |x_2(n-m)|^{i-j} |x_1(n-m)|^j \end{aligned} \quad (11)$$

in which $c_{1,mij}$ and $c_{2,mij}$ are the complex coefficients of the polynomials of order K. We note that (11) is in general only valid around the two carrier frequencies and is not able to predict (or correct) the out-of-band intermodulation products. However, in the following characterization of the DB-PA, only narrowband pulses (e.g., 10-μs duration) will be employed; therefore, it is possible to discard the memory part of the model (11) by setting $M = 0$. This results in a very compact form of (10) that does not depend on the previous samples

$$\begin{bmatrix} y_1 \\ y_2 \end{bmatrix} = \begin{bmatrix} \hat{G}_{11}(|x_1|, |x_2|) & \hat{G}_{12}(|x_1|, |x_2|) \\ \hat{G}_{21}(|x_1|, |x_2|) & \hat{G}_{22}(|x_1|, |x_2|) \end{bmatrix} \begin{bmatrix} x_1 \\ x_2 \end{bmatrix}. \quad (12)$$

If we express (12) in terms of input and output powers in place of the envelopes, this results in

$$\begin{bmatrix} P_{O1} \\ P_{O2} \end{bmatrix} = \begin{bmatrix} |G_{11}(P_{I1}, P_{I2})| & |G_{12}(P_{I1}, P_{I2})| \\ |G_{21}(P_{I1}, P_{I2})| & |G_{22}(P_{I1}, P_{I2})| \end{bmatrix} \begin{bmatrix} P_{I1} \\ P_{I2} \end{bmatrix}. \quad (13)$$

In particular, G_{11} and G_{22} are the direct gains between corresponding input–output ports, while G_{12} and G_{21} represent the cross-gains from ports 1 to 2 and from ports 2 to 1. Equation (13) is used in this paper for characterizing the DB-PA in various modes of operation.

ACKNOWLEDGMENT

Modelithics models are utilized under the University License Program from Modelithics, Inc., Tampa, FL, USA. The authors would like to thank Prof. A. Cappello, University of Bologna, Bologna, Italy, for advising the development of the signal generation algorithm.

REFERENCES

[1] M. Shafi *et al.*, "5G: A tutorial overview of standards, trials, challenges, deployment, and practice," *IEEE J. Sel. Areas Commun.*, vol. 35, no. 6, pp. 1201–1221, Jun. 2017.

[2] S.-Y. Lien, S.-L. Shieh, Y. Huang, B. Su, Y.-L. Hsu, and H.-Y. Wei, "5G new radio: Waveform, frame structure, multiple access, and initial access," *IEEE Commun. Mag.*, vol. 55, no. 6, pp. 64–71, Jun. 2017.

[3] I. F. Akyildiz, S. Nie, S.-C. Lin, and M. Chandrasekaran, "5G roadmap: 10 key enabling technologies," *Comput. Netw.*, vol. 106, pp. 17–48, Sep. 2016.

[4] M. Agiwal, A. Roy, and N. Saxena, "Next generation 5G wireless networks: A comprehensive survey," *IEEE Commun. Surveys Tuts.*, vol. 18, no. 3, pp. 1617–1655, 3rd Quart., 2016.

[5] Qualcomm. (Dec. 2016). *Making 5G NR a Reality: Leading the Technology Inventions for a Unified, More Capable 5G Air Interface*. Accessed: Dec. 2018. [Online]. Available: https://www.qualcomm.com/media/documents/files/whitepaper-making-5g-nr-a-reality.pdf

[6] C. S. Park, L. Sundström, A. Wallén, and A. Khayrallah, "Carrier aggregation for LTE-advanced: Design challenges of terminals," *IEEE Commun. Mag.*, vol. 51, no. 12, pp. 76–84, Dec. 2013.

[7] A. Kiayani, V. Lehtinen, L. Anttila, T. Lahteensuo, and M. Valkama, "Linearity challenges of LTE-advanced mobile transmitters: Requirements and potential solutions," *IEEE Commun. Mag.*, vol. 55, no. 6, pp. 170–179, Jun. 2017.

[8] N. Kelly, W. Cao, and A. Zhu, "Preparing linearity and efficiency for 5G: Digital predistortion for dual-band Doherty power amplifiers with mixed-mode carrier aggregation," *IEEE Micro. Mag.*, vol. 18, no. 1, pp. 76–84, Feb. 2017.

[9] H. Zou, Y. Li, H. Shen, H. Wang, and G. Yang, "Design of 6 × 6 dual-band MIMO antenna array for 4.5G/5G smartphone applications," in *Proc. 6th Asia–Pacific Conf. Antennas Propag. (APCAP)*, Oct. 2017, pp. 1–3.

[10] A. A. Zaidi *et al.*, "Waveform and numerology to support 5G services and requirements," *IEEE Commun. Mag.*, vol. 54, no. 11, pp. 90–98, Nov. 2016.

[11] Q.-F. Cheng, H.-P. Fu, S.-K. Zhu, and J.-G. Ma, "Two-stage high-efficiency concurrent dual-band harmonic-tuned power amplifier," *IEEE Trans. Microw. Theory Techn.*, vol. 64, no. 10, pp. 3232–3243, Oct. 2016.

[12] J. Pang, S. He, C. Huang, Z. Dai, C. Li, and J. Peng, "A novel design of concurrent dual-band high efficiency power amplifiers with harmonic control circuits," *IEEE Microw. Wireless Compon. Lett.*, vol. 26, no. 2, pp. 137–139, Feb. 2016.

[13] H. Sarbishaei, Y. Hu, B. Fehri, and S. Boumaiza, "Concurrent dual-band envelope tracking power amplifier for carrier aggregated systems," in *IEEE MTT-S Int. Microw. Symp. Dig.*, Jun. 2014, pp. 1–4.

[14] M. R. Duffy, G. Lasser, J. Vance, M. Olavsbråten, T. Barton, and Z. Popovic, "Bandwidth-reduced supply modulation of a high-efficiency X-band GaN MMIC PA for multiple wideband signals," in *IEEE MTT-S Int. Microw. Symp. Dig.*, Jun. 2017, pp. 1850–1853.

[15] C. Sánchez-Pérez, M. Özen, C. M. Andersson, D. Kuylenstierna, N. Rorsman, and C. Fager, "Optimized design of a dual-band power amplifier with SiC varactor-based dynamic load modulation," *IEEE Trans. Microw. Theory Techn.*, vol. 63, no. 8, pp. 2579–2588, Aug. 2015.

[16] A. Duh, S. Rahimizadeh, T. Barton, and Z. Popović, "A 3.5/5.9-GHz dual-band output matching network for an efficiency-optimized multiband power amplifier," in *Proc. IEEE Topical Conf. Power Amplif. Wireless Radio Appl.*, Jan. 2018, pp. 1–4.

[17] M. Liu, H. Golestaneh, and S. Boumaiza, "A concurrent 2.15/3.4 GHz dual-band Doherty power amplifier with extended fractional bandwidth," *IEEE MTT-S Int. Microw. Symp. Dig.*, May 2016, pp. 15–17.

[18] X. Chen, W. Chen, G. Su, F. M. Ghannouchi, and Z. Feng, "A concurrent dual-band 1.9–2.6-GHz Doherty power amplifier with Intermodulation impedance tuning," *IEEE MTT-S Int. Microw. Symp. Dig.*, Jun. 2014, pp. 6–9.

[19] P. Saad, P. Colantonio, L. Piazzon, F. Giannini, K. Andersson, and C. Fager, "Design of a concurrent dual-band 1.8–2.4-GHz GaN-HEMT Doherty power amplifier," *IEEE Trans. Microw. Theory Techn.*, vol. 60, no. 6, pp. 1840–1849, Jun. 2012.

[20] W. Chen, S. Zhang, Y. Liu, Y. Liu, and F. Ghannouchi, "A concurrent dual-band uneven Doherty power amplifier with frequency-dependent input power division," *IEEE Trans. Circuits Syst. I, Reg. Papers*, vol. 61, no. 2, pp. 552–561, Feb. 2014.

[21] Y. Sun, X.-W. Zhu, J. Zhai, L. Zhang, and F. Meng, "Highly efficient concurrent power amplifier with controllable modes," *IEEE Trans. Microw. Theory Techn.*, vol. 63, no. 12, pp. 4051–4060, Dec. 2015.

[22] W. Chen *et al.*, "Design and linearization of concurrent dual-band Doherty power amplifier with frequency-dependent power ranges," *IEEE Trans. Microw. Theory Techn.*, vol. 59, no. 10, pp. 2537–2546, Oct. 2011.

[23] S. Yamanouchi, K. Kunihiro, and M. Ikekawa, "A concurrent dual-band/multi-carrier transmitter architecture for power and efficiency enhancement," in *IEEE MTT-S Int. Microw. Symp. Dig.*, Jun. 2013, pp. 3–5.

[24] K. Rawat and F. M. Ghannouchi, "Design methodology for dual-band Doherty power amplifier with performance enhancement using dual-band offset lines," *IEEE Trans. Ind. Electron.*, vol. 59, no. 12, pp. 4831–4842, Dec. 2012.

[25] X. Chen, W. Chen, F. M. Ghannouchi, Z. Feng, and Y. Liu, "Enhanced analysis and design method of concurrent dual-band power amplifiers with intermodulation impedance tuning," *IEEE Trans. Microw. Theory Techn.*, vol. 61, no. 12, pp. 4544–4558, Dec. 2013.
[26] Y. Liu, P. Roblin, H. Yu, S. Shao, and Y. Tang, "Novel multiband linearization technique for closely-spaced dual-band signals of wide bandwidth," in *IEEE MTT-S Int. Microw. Symp. Dig.*, May 2015, pp. 1–4.
[27] T. Xu and I. Darwazeh, "Transmission experiment of bandwidth compressed carrier aggregation in a realistic fading channel," *IEEE Trans. Veh. Technol.*, vol. 66, no. 5, pp. 4087–4097, May 2017.
[28] R. Ma, K. H. Teo, S. Shinjo, K. Yamanaka, and P. M. Asbeck, "A GaN PA for 4G LTE-advanced and 5G: Meeting the telecommunication needs of various vertical sectors including automobiles, robotics, health care, factory automation, agriculture, education, and more," *IEEE Microw. Mag.*, vol. 18, no. 7, pp. 77–85, Nov. 2017.
[29] S. H. Han and J. H. Lee, "An overview of peak-to-average power ratio reduction techniques for multicarrier transmission," *IEEE Wireless Commun.*, vol. 12, no. 2, pp. 56–65, Apr. 2005.
[30] G. K. Srivastava and N. K. Tadkapalli, "Crest factor reduction for carrier aggregated OFDM systems," in *Proc. 20th Int. Conf. Softw., Telecommun. Comput. Netw. (SoftCOM)*, Sep. 2012, pp. 1–6.
[31] C. Zhao, R. J. Baxley, G. T. Zhou, D. Boppana, and J. S. Kenney, "Constrained clipping for crest factor reduction in multiple-user OFDM," in *Proc. IEEE Radio Wireless Symp.*, Jan. 2007, pp. 341–344.
[32] S. H. Müller and J. B. Huber, "OFDM with reduced peak-to-average power ratio by optimum combination of partial transmit sequences," *Electron. Lett.*, vol. 33, no. 5, pp. 368–369, Feb. 1997.
[33] R. J. Baxley and G. T. Zhou, "Comparing selected mapping and partial transmit sequence for PAR reduction," *IEEE Trans. Broadcast.*, vol. 53, no. 4, pp. 797–803, Dec. 2007.
[34] C. Florian, T. Cappello, R. P. Paganelli, D. Niessen, and F. Filicori, "Envelope tracking of an RF high power amplifier with an 8-level digitally controlled GaN-on-Si supply modulator," *IEEE Trans. Microw. Theory Techn.*, vol. 63, no. 8, pp. 2589–2602, Aug. 2015.
[35] T. Cappello, T. W. Barton, C. Florian, M. Litchfield, and Z. Popović, "Multilevel supply-modulated Chireix outphasing with continuous input modulation," *IEEE Trans. Microw. Theory Techn.*, vol. 65, no. 12, pp. 5231–5243, Dec. 2017.
[36] D. Palmisano *et al.*, "Multisine decomposition algorithm for RF power amplifier characterization," in *Proc. MTT-S Int. Microw. RF Conf. (IMaRC)*, Dec. 2015, pp. 49–52.
[37] N. B. Carvalho, K. A. Remley, D. Schreurs, and K. G. Card, "Multisine signals for wireless system test and design [application notes]," *IEEE Microw. Mag.*, vol. 9, no. 3, pp. 122–138, Jun. 2008.
[38] J. C. Pedro and N. B. Carvalho, "Designing multisine excitations for nonlinear model testing," *IEEE Trans. Microw. Theory Techn.*, vol. 53, no. 1, pp. 45–54, Jan. 2005.
[39] M. Li, K. M. Gharaibeh, K. G. Gard, and M. B. Steer, "Accurate multisine representation of digital communication signals for characterization of nonlinear circuits," in *Proc. IEEE Radio Wireless Symp.*, Jan. 2006, pp. 527–530.
[40] S. Narahashi and T. Nojima, "New phasing scheme of N-multiple carriers for reducing peak-to-average power ratio," *Electron. Lett.*, vol. 30, no. 17, pp. 1382–1383, Aug. 1994.
[41] N. R. Draper and H. Smith, *Applied Regression Analysis*. Hoboken, NJ, USA: Wiley, 1998.
[42] T. Cappello, P. Pednekar, C. Florian, S. Cripps, Z. Popović, and T. Barton, "Supply- and load-modulated balanced amplifier for efficient broadband 5G base stations," *IEEE Trans. Microw. Theory Techn.*, to be published.
[43] G. L. Matthaei, "Tables of Chebyshev impedance–transforming networks of low-pass filter form," *Proc. IEEE*, vol. 52, no. 8, pp. 939–963, Aug. 1964.
[44] C. Florian, T. Cappello, A. Santarelli, D. Niessen, F. Filicori, and Z. Popović, "A prepulsing technique for the characterization of GaN power amplifiers with dynamic supply under controlled thermal and trapping states," *IEEE Trans. Microw. Theory Techn.*, vol. 65, no. 12, pp. 5046–5062, Dec. 2017.
[45] D. R. Morgan, Z. Ma, J. Kim, M. G. Zierdt, and J. Pastalan, "A generalized memory polynomial model for digital predistortion of RF power amplifiers," *IEEE Trans. Signal Process.*, vol. 54, no. 10, pp. 3852–3860, Oct. 2006.
[46] S. A. Bassam, F. M. Ghannouchi, and M. Helaoui, "2-D digital predistortion (2-D-DPD) architecture for concurrent dual-band transmitters," *IEEE Trans. Microw. Theory Techn.*, vol. 59, no. 10, pp. 2547–2553, Oct. 2011.

Tommaso Cappello (S'13–M'17) received the Laurea degree *(cum laude)* in electrical engineering and the Ph.D. degree from the University of Bologna, Bologna, Italy, in 2013 and 2017, respectively.

Since 2017, he has been with a Research Associate with the Microwave and RF Research Group, University of Colorado Boulder, Boulder, CO, USA. His current research interests include the design, characterization, and modeling of RF power amplifiers in efficient transmitters for radar and communications, and high-voltage gallium-nitride device characterization and modeling for power electronics.

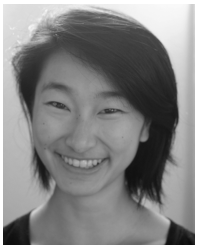

Allison Duh (S'16) received the B.S.E.E. degree from Columbia University, New York, NY, USA, in 2014, and the M.S.E.E. degree from the University of Colorado Boulder, Boulder, CO, USA, in 2018, where she is currently pursuing the Doctorate degree with a focus on concurrent multiband and reconfigurable amplifier design.

In 2015, she joined the Technical University of Munich, Munich, Germany, as a Visiting Research Student.

Taylor Wallis Barton (S'07–M'12) received the Sc.B., M.Eng., E.E., and Sc.D. degrees from the Massachusetts Institute of Technology, Cambridge, MA, USA.

She was a Post-Doctoral Associate with the MIT Microsystems Technology Laboratories, University of Texas at Dallas, Richardson, TX, USA, where she became an Assistant Professor. In 2016, she joined the Department of Electrical, Computer, and Energy Engineering, University of Colorado Boulder, Boulder, CO, USA, where she is currently an Assistant Professor and holds the Lockheed Martin Faculty Fellowship for Outstanding Junior Faculty.

Dr. Barton was a recipient of the AFOSR Young Investigator Award and the NSF CAREER Award.

Zoya Popovic (S'86–M'90–SM'99–F'02) received the Dipl.Ing. degree from the University of Belgrade, Belgrade, Serbia, and the Ph.D. degree with the California Institute of Technology, Pasadena, CA, USA.

From 2001 to 2003 and in 2014, she was a Visiting Professor with the Technical University of Munich, Munich, Germany, and ISAE, Toulouse, France. She has graduated 58 Ph.D. students and currently advises 12 doctoral students. She is currently a Distinguished Professor and the Lockheed Martin Endowed Chair of Electrical Engineering with the University of Colorado Boulder, Boulder, CO, USA. Her current research interests include high-efficiency power amplifiers and transmitters, microwave and millimeter-wave high-performance circuits for communications and radar, medical applications of microwaves, millimeter-wave, and terahertz quasi-optical techniques, and wireless powering.

Dr. Popovic was a recipient of two IEEE MTT-S Microwave Prizes for best journal papers, the White House NSF Presidential Faculty Fellow Award, the URSI Issac Koga Gold Medal, the ASEE/HP Terman Medal, and the German Humboldt Research Award. She was elected as a Foreign Member of the Serbian Academy of Sciences and Arts in 2006. She was named as the IEEE MTT-S Distinguished Educator in 2013 and the University of Colorado Distinguished Research Lecturer in 2015. She was named as a Chair of Excellence at the Carlos III University of Madrid in 2018.